Hang Li[ab]*, Zhe Gao[c], Xingxing Bai[d], Yongming Jin[d], Xianglong Meng[e], Wei Cai[e], Jin-Yoo Suh[f] and Jae-il Jang[c]

[a]School of Energy and Materials, Shihezi University, Shihezi, China; [b]Institute of Bingtuan Energy Development Research, Shihezi University, Shihezi, China; [c]Division of Materials Science and Engineering, Hanyang University, Seoul, Republic of Korea; [d]Analysis and Testing Center, Xinjiang University, Urumqi, China; [e]School of Materials Science and Engineering, Harbin Institute of Technology, Harbin, China; [f]Center for Energy Materials Research, Korea Institute of Science and Technology, Seoul, Republic of Korea

*corresponding author: Hang Li, Ph.D., Associate Professor, School of Energy and Materials, Shihezi University, Shihezi, China, e-mail: lihanglihang2002@163.com

# High-strength gradient Ti-Ni-Cu-Pd ribbon with large recoverable strain and high cyclic stability under load


## Abstract

Bulk Ti–Ni–Cu–Pd alloys show decent thermal- and load-cycling stability, yet low strength and limited recoverable strain. Here, we design a gradient Ti–Ni–Cu–Pd ribbon via nanoscale dual-phase (nanocrystalline–amorphous) engineering. The ribbon achieves 1–2× higher strength than bulk austenite while delivering ~4% fully recoverable strain (bulk well below 3%). Under high load, the strain amplitude declines only 0.5–0.7% after 10 loading cycles, demonstrating exceptional cyclic stability. These properties arise from phase synergy across the gradient architecture, enabling compact, high-force, repeatable actuators.



Keywords: Shape memory alloys; recoverable strain; cyclic stability; nanoindentation


## Introduction

Shape memory alloys (SMAs), as intelligent metallic biomimetic materials, have shown great potential in integrated actuation and sensing applications. Relying on their solid-state phase transformation mechanism, SMAs can achieve large recoverable strains without the need for complex mechanical systems and have been widely applied in aerospace, electronics, and biomedical fields [1,2]. Among them, Ti-Ni alloys are the most commonly used commercial SMA system [3-11]. However, Ti-Ni alloys exhibit a relatively wide transformation temperature hysteresis, approximately 25-40 °C, resulting in low sensitivity and slow response speed when used as actuator materials. Moreover, repeated thermal or stress cycling leads to the degradation of functional properties, thereby compromising the overall functional stability [12-14].

Prior studies indicate that partially substituting Ni with Cu in Ti–Ni alloys does not change the crystal structure of the parent phase; even at 30 at.% Cu, the parent phase remains B2 [15]. With increasing Cu content, the transformation (thermal)

hysteresis tends to decrease [16]. At 5, 12.5, and 20 at.% Cu, the hysteresis widths are ~19 °C, 11 °C, and 8 °C, respectively, leaving substantial room for further reduction. Guided by the geometrically nonlinear theory of martensite (GNLTM), extensive searches in Ti–Ni–Cu alloys with high Cu (⩾15 at.%) have not identified compositions exhibiting near-zero thermal hysteresis [17,18]. Subsequent quaternary alloying shows that, in stoichiometric Ti–Ni–Cu–Pd alloys, when $\lambda_2$ is very close to 1, the transformation hysteresis is markedly reduced toward near-zero [19], while the alloys simultaneously exhibit robust elastocaloric fatigue performance [20]. Using GNLTM, Ti-Ni-Cu-Pd ultra-narrow hysteresis memory alloys with off-stoichiometric composition were designed and fabricated. By adjusting the Pd content, the lattice parameters were effectively tuned to make the $\lambda_2$ value approach unity, resulting in ultra-narrow hysteresis, and a relationship between ultra-narrow hysteresis and high thermal cycling stability was established [21,22]. Furthermore, 5000 thermal cycles was conducted on the selected Ti-Ni-Cu-Pd alloy composition, and the variation of transformation temperature throughout the cycles was less than 1 °C, demonstrating extraordinary thermal cycling stability [23], and the key mechanism for this high thermal cycling stability was revealed. Due to the difficulty in introducing dislocations during thermal cycling, the alloy also exhibited a unique and repeatable temperature memory effect after undergoing incomplete thermal training [24]. Additionally, it was further reported that the Ti-Ni-Cu-Pd ultra-narrow hysteresis memory alloy also exhibited high cycling stability in both shape memory effect and hysteresis (slightly larger than that under thermal field alone) under applied stress, and its mechanism was attributed to the difficulty in introducing dislocations during stress cycling [25]. However, it was also found that due to the relatively low strength of the Ti-Ni-Cu-Pd

ultra-narrow hysteresis memory alloy, the fully recoverable strain in the austenitic state is far less than 3%.

In the past decades, grain refinement and amorphization have been the main approaches for developing high-performance materials, and combining different microstructural phases at the nanoscale has become a new method to achieve such performance. Bulk metallic glasses in the amorphous state possess high strength, but their recoverable strain is limited (with a theoretical elastic limit around 2%) [26-28], and they are prone to deformation through localized shear bands [29-31]. However, nanoscale metallic glass specimens can exhibit large recoverable strains and enhanced resistance to shear bands [32]. Similarly, reducing grain size to the nanoscale can significantly suppress transformation-induced dislocations in crystalline SMAs [33,34]. As previously mentioned, crystalline Ti-Ni-Cu-Pd ultra-narrow hysteresis memory alloys suffer from low strength and poor resistance to dislocation slip. Therefore, in this study, we propose using melt-spinning as the preparation method to obtain a gradient nanocomposite Ti-Ni-Cu-Pd memory alloy ribbon with a heterogeneous multiphase nanostructure of critical dimension, in which crystalline and amorphous phases can synergistically improve strength, recoverable strain, and fatigue resistance.

**Experimental**

The sample utilized here is an as-spun $Ti_{48.5}Ni_{34.5}Cu_{11.5}Pd_{5.5}$ ribbon (with a linear velocity of 55 m/s on the surface of spinning wheel). Grazing-incidence X-ray diffraction (GI-XRD; Rigaku, SmartLab SE) patterns were acquired at room temperature on the air and roll sides of ribbons over identical areas, using incident angles of 0.5°, 1°, and 2°. Nanoindentation experiments were performed at room temperature using the Nanoindenter-XP (KLA) instrument with a Berkovich indenter and a spherical indenter with tip radius, $R$, of 1.84 μm (determined by Hertzian contact

analysis of indentations on fused quartz samples). All the probed surfaces were vibration-polished with 0.02 μm colloidal silica. More than 10 indentations were conducted for each condition. The microstructures of the specimens were examined using TEM (JEOL, JEM-F200). Ion milling (IM; Gatan, Gatan 695 (PIPS II)) milling was performed to obtain TEM samples from both the roll and air sides of the ribbons.

**Results and Discussion**

GI-XRD patterns were collected at fixed incident angles (α = 0.5°, 1.0°, 2.0°) for both the roll and air sides of the as-spun $Ti_{48.5}Ni_{34.5}Cu_{11.5}Pd_{5.5}$ ribbon, as shown in Figs. 1a-b. A comparison of the diffraction profiles reveals clear differences in microstructural characteristics between the two sides. The roll side exhibits broad amorphous halos superimposed with sharp crystalline reflections corresponding to the B2 austenite phase, whereas the air side displays sharper B2 peaks with a weaker amorphous contribution. After instrument background subtraction, each pattern $I(2\theta)$was decomposed into an amorphous halo and crystalline contributions. The amorphous component was modeled by a Gaussian hump plus constant offset, $B(2\theta) = c + A\exp\left[-\frac{(2\theta-\mu)^2}{2\sigma^2}\right]$, fitted by least squares over 28–52° while excluding windows around crystalline reflections to avoid peak bias. The integration windows used for crystalline peaks were centered at the B2 reflections near 42° $(110)$, 62° $(200)$and 77° $(211)$; specifically, 41.2–43.0°, 61.3–63.3° and 76.0–78.5°. The amorphous area was taken as $A_a = \int_{20^\circ}^{80^\circ} B(2\theta)\, d(2\theta)$, and the crystalline area as the sum of positive residuals above the fitted halo within the peak windows, $A_c = \sum_{\text{windows}} \int \max\left(I(2\theta) - B(2\theta), 0\right) d(2\theta)$. Numerical integration used the trapezoidal rule. The crystallinity was then calculated as $X_c = \frac{A_c}{A_c + A_a}$. Using this procedure, the resulting crystallinity values for the roll side at α = 0.5°, 1.0°, and 2.0° are

approximately 6.5%, 8.9%, and 10.1%, respectively. For the air side, the corresponding crystallinity values at α = 0.5°, 1.0°, and 2.0° are 46.7%, 42.1%, and 35.3%, respectively. Although the crystalline domains on both sides are within the nanocrystalline scale, the size discrepancy primarily arises from differences in cooling rates during melt spinning. Taken together, these results confirm that the ribbon possesses a dual-phase architecture comprising both amorphous and crystalline components, with a pronounced through-thickness gradient in phase distribution. Figs. 1c–d present the HRTEM characterization of the roll side and air side, respectively. Consistent with the GI-XRD analysis, the roll side is dominated by an amorphous matrix within which nanoscale short-range-ordered (SRO) domains are dispersed. Masked fast Fourier transforms (FFTs) and inverse masked FFT reconstructions performed on the boxed regions demonstrate that these domains are crystalline (Fig. 1c). In contrast, the crystalline phase fraction is markedly higher on the air side; combining FFT-derived electron diffraction patterns (EDPs) with inverse masked FFT reconstructions of the boxed regions enables an unambiguous assignment of the crystalline phase to B2 austenite (Fig. 1d). Notably, Fig. 1d also provides direct evidence that dislocation slip is suppressed at amorphous–crystalline interfaces.

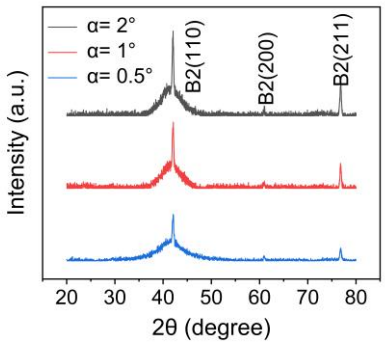


(a)

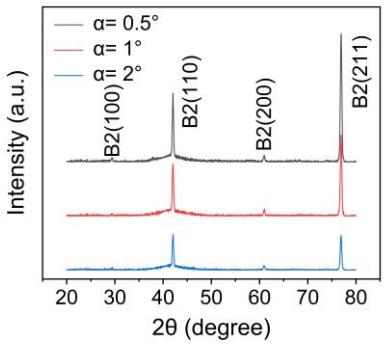


(b)

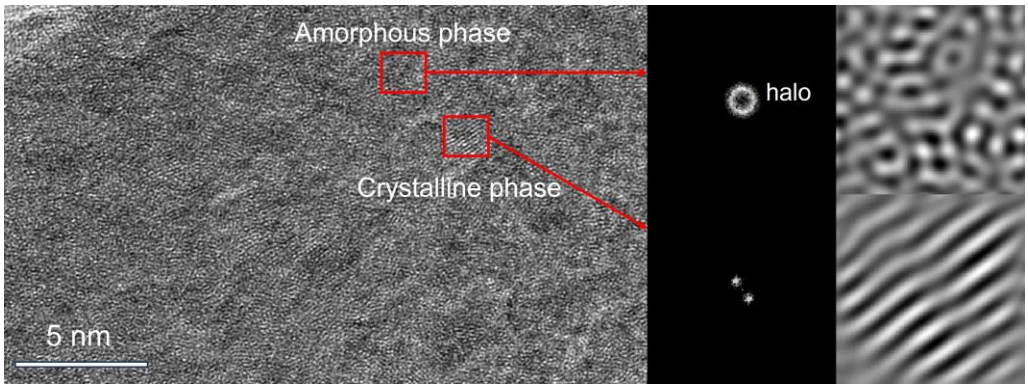


(c)

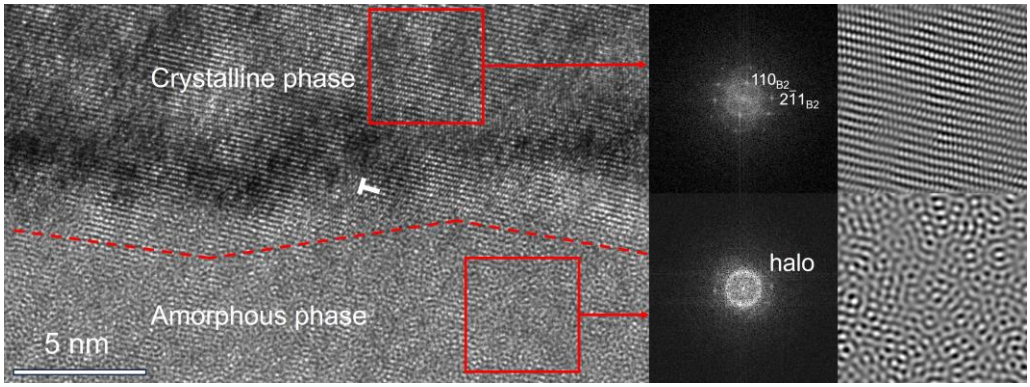


(d)

Fig. 1. GI-XRD patterns of as-spun $Ti_{48.5}Ni_{34.5}Cu_{11.5}Pd_{5.5}$ ribbon: (a) roll-side, (b) air-side. (c) HRTEM image, masked fast Fourier transform images and inverse masked fast Fourier transform images of the boxed regions from roll side. (d) HRTEM image, corresponding EDPs calculated by FFT method and inverse masked fast Fourier transform images of the boxed regions from air-side.

Based on the above analysis, a schematic of the through-thickness gradient architecture can be constructed (as shown in Fig. 2a). The rectangle represents a cross-section through the ribbon thickness. The gray field denotes the amorphous matrix, and the black polygons represent crystalline domains (symbolic shapes, not to scale). From the roll side (wheel-contact surface) toward the air side (free surface), both the volume fraction and characteristic size of the crystalline phase increase, while the region near the roll side remains amorphous-rich with finer, more sparsely distributed crystallites. The vertical arrow marks the thickness direction. This schematic is intended to convey the qualitative gradient that underpins the microstructural interpretation; it does not imply specific particle shapes, orientations, or exact number densities. A detailed

nanoindentation investigation of the roll side and air side of the as-spun $Ti_{48.5}Ni_{34.5}Cu_{11.5}Pd_{5.5}$ ribbon reveals distinct mechanical behaviors between the two surfaces. Compared to its bulk austenitic counterpart, both sides exhibit significantly enhanced strength—approximately 2 to 3 times that of the bulk alloy—with the roll side demonstrating ~15% greater strength than the air side. Quantitative comparison with existing high-strength NiTi alloys—nanocrystalline austenitic NiTi ($H \approx 4.5$ GPa) [35] and austenitic NiTi thin films ($H \approx 4.2$ GPa) [36]—further highlights the high strength of the present ribbon. Analysis of the strain rate sensitivity index m indicates slightly reduced plasticity on the roll side relative to the air side (Fig. 2b). Notably, the *P–h* curve for the roll side show pronounced pop-in events (Fig. 2c), a phenomenon rarely observed in nanoindentation studies of SMAs, as supported by our previous work [37-39]. The occurrence of pop-in events points to a substantially higher fraction of the amorphous phase on the roll side compared to the air side, and it also underscores the exceptional elastic behavior of these amorphous regions under high strain (>4%, far exceeding the theoretical elastic limit of bulk metallic glasses [26-28]; see Fig. 3). In crystal–amorphous coexisting systems, intermixing can generate nanoscale amorphous regions, thereby raising the recoverable elastic strain of the amorphous fraction to >2%. By contrast, in crystalline Ti–Ni–Cu-based alloys the purely elastic, fully recoverable strain typically lies at ~0.4–1%; grain refinement affords only limited gains (commonly from ~0.4% to ~0.8–1%), far below the substantial increases achievable via pseudoelasticity. Furthermore, as shown in the inset of Fig. 2c, a representative nanoindentation *P–h* curve obtained at 3 mN without pop-in (corresponding to the amorphous phase in its elastic regime) exhibits pronounced hysteresis—the unloading path does not retrace the loading path—indicating that the response is not purely elastic. Accordingly, the nanoindentation *P–h* curve is more reasonably attributed to a

combination of elastic deformation and stress-induced martensitic transformation (SIMT). Remarkably, the pop-in onset far exceeds the typical elastic limit of conventional amorphous phases, implying that in the presence of crystalline phases, the amorphous domains can sustain larger strains without yielding. This suggests a reinforcing effect of the crystalline phase on the elastic response of the amorphous phase. Furthermore, the unique mechanical behavior observed on the roll side provides compelling evidence for the presence of a gradient microstructure within the ribbon, corroborating findings from prior GI-XRD and HRTEM analysis.

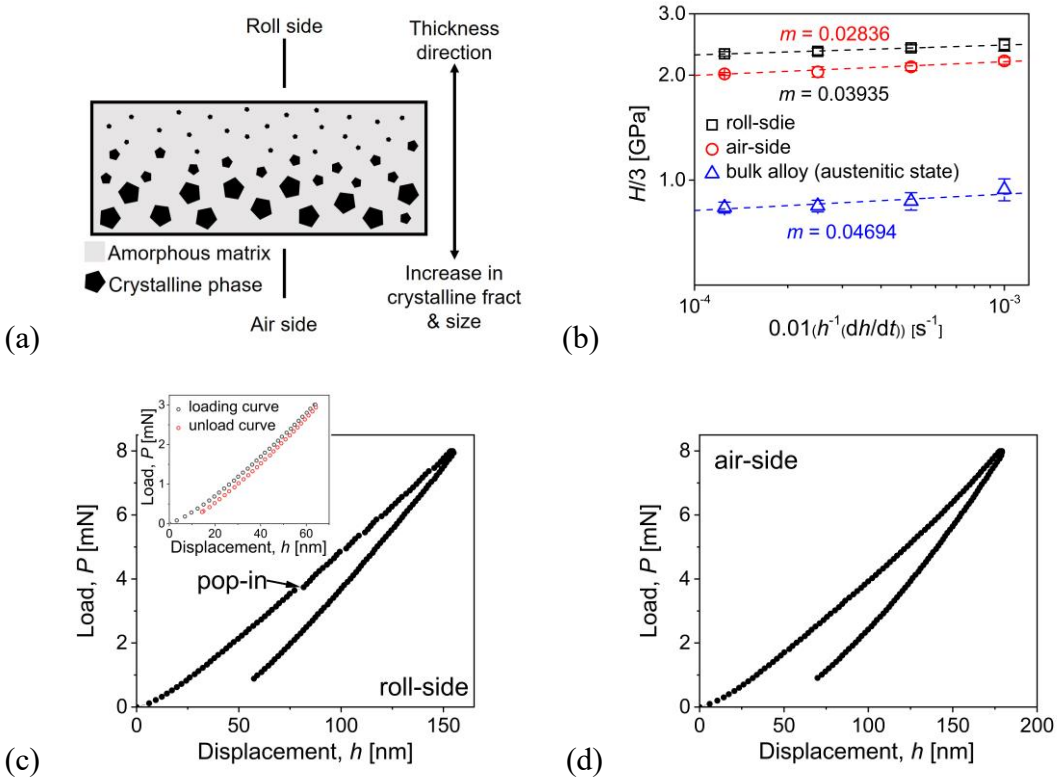


Fig. 2. (a) Schematic of the through-thickness gradient architecture. (b) Stress vs. strain rate. Representative *P*–*h* curves: (c) roll-side (with inset showing a representative 3 mN *P*–*h* curve without pop-in), (d) air-side.

As established in our previous study [37], spherical indentation generates a stress/strain field with a non-uniform gradient distribution. In the high-stress region beneath the indenter, localized plastic deformation arises from the combined

contributions of geometrically necessary dislocations (GNDs), statistically stored dislocations (SSDs) within stress-induced martensite, and phase transformation dislocations (PTDs). In contrast, in the deeper low-stress regions, plastic deformation is unlikely to occur due to the insufficient stress to reach the yield strength of stress-induced martensite and the significant reduction or complete absence of GNDs with increasing depth. Spherical nanoindentation with a tip radius of 34.94 μm yields nearly complete strain recovery under 4% strain. In contrast, using a smaller tip with a radius of 1.84 μm results in an unrecovered strain of approximately 15% at the same strain level. This pronounced size effect originates from the evolution of dislocation structures within the high-stress zone during nanoindentation: the synergistic generation and co-accumulation of GNDs, a small amount of SSDs, and a small amount of PTDs lead to the irreversible formation of localized residual strain. Among these mechanisms, the density of GNDs plays a dominant role and is strongly dependent on the indenter radius. A larger radius leads to a lower GND density, and as the radius approaches infinity, GNDs effectively vanish. Under this condition, the strain recovery behavior of spherical nanoindentation converges with that observed under macroscopic uniaxial loading. Therefore, a recovery ratio of ~85% obtained at 4% strain using a spherical indenter with a radius of 1.84 μm can be considered equivalent to full recovery under conventional uniaxial testing conditions.

A comparison of the recovery ratios between the roll side and air side of the as-spun $Ti_{48.5}Ni_{34.5}Cu_{11.5}Pd_{5.5}$ ribbon under various indentation loads and strain levels using a spherical indenter with a radius of 1.84 μm (Fig. 3) reveals that the roll side achieves a recovery ratio as high as ~90% at a strain of ~4%, indicating a relatively high amorphous phase fraction on this side. At this strain level, the stress in the high-stress region remains below the yield strength of the amorphous phase (Fig. 2b), allowing only

reversible short-range atomic rearrangements (e.g., transient formation of shear transformation zones) within the amorphous domains. Meanwhile, GNDs and a small amount of SSDs are generated in the crystalline regions, with PTDs being negligible in this alloy system. These mechanisms collectively contribute to the high recovery ratio. As the load increases, plastic deformation begins to occur in the amorphous phase, leading to a linear decrease in the recovery ratio. This trend also reflects the influence of SSDs within the crystalline phase in the low-stress regions of the indentation field, potentially resulting in even lower recovery ratios at comparable strain levels (~6–7%). The air side, having a lower amorphous content, exhibits deformation behavior more akin to conventional superelastic SMAs. The unrecovered strain of ~15% at ~4% total strain is primarily attributed to GNDs and a small amount of SSDs within the high-stress crystalline region. As the strain increases, plastic deformation initiates in the amorphous phase, along with the formation of SSDs in stress-induced martensite within the low-stress zones. Overall, at ~4% strain, the residual strain on both sides primarily originates from GNDs and a small amount of SSDs in the high-stress crystalline regions—an intrinsic feature of nanoindentation. These results correspond to a fully recoverable state under macroscopic uniaxial loading. Notably, the maximum recoverable strain on both surfaces significantly exceeds that of the bulk Ti-Ni-Cu-Pd alloy, which exhibits irreversible deformation under macroscopic loading at strains well below 3% [25]. As previously mentioned, nanoscale structural refinement provides significant advantages in both amorphous and crystalline alloys. In metallic glasses, it enhances recoverable strain and mitigates shear band propagation [32], while in SMAs, it effectively suppresses transformation-induced dislocation activity [33,34]. In the present ribbon, the superior recoverability arises not only from the aforementioned effects but, more importantly, from a nanoscale dual-phase architecture in which

crystalline domains are embedded in—and strongly constrained by—a high-strength amorphous matrix (Fig. 1c). Consistent with this, Fig. 1d provides direct evidence that dislocation slip is suppressed at amorphous–crystalline interfaces. To make the mechanism explicit, we added a schematic (Fig. 3c) to clarify the mechanism: the amorphous matrix constrains the crystalline domains—reducing dislocation and grain-boundary motion—whereas the crystals confine the amorphous regions, blocking shear-band formation and advance.

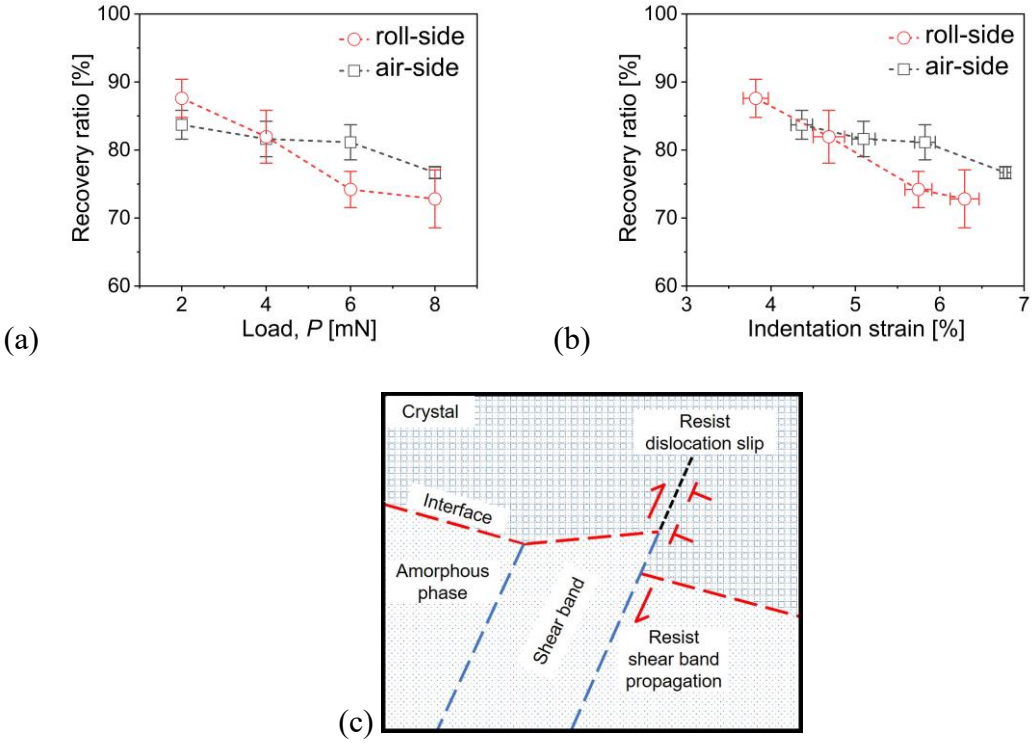


Fig. 3. Depth recovery ratio as a function of the maximum indentation load (a) and strain (b). (c) Schematic illustrating how two-phase synergy constrains shear band propagation in the amorphous matrix and curbs dislocation slip within the crystals.

Both the roll side and the air side of the as-spun $Ti_{48.5}Ni_{34.5}Cu_{11.5}Pd_{5.5}$ ribbon exhibit exceptional stability under cyclic nanoindentation loading. As shown in Fig. 4, a constant load of 3 mN is applied, corresponding to strains of approximately 4.4% for the roll side and 4.9% for the air side. From the perspective of energy dissipation—which primarily arises from incompatibility across phase boundaries during

transformation—both sides show only minimal reductions in dissipated energy over ten cycles, indicating low energy loss. Notably, the roll side exhibits an even smaller decline in dissipated energy, decreasing by only 8% after ten cycles. In stark contrast, our previous study on Ti-Ni superelastic alloy shows a 70% reduction under identical cyclic times [37]. This performance of the roll side likely results from its higher fraction of the amorphous phase, which remains largely below the threshold for plastic deformation during cyclic loading, thus contributing negligibly to energy dissipation. Furthermore, the crystalline domains on the roll side exhibit excellent phase compatibility, limiting additional energy losses during phase transformation. Importantly, the amorphous regions also suppress dislocation nucleation and glide within the crystalline phases, further enhancing the functional stability of the ribbon. After ten loading cycles, the residual strain degradation on the roll side amounts to merely 0.5% of the initial cyclic strain (Fig. 4b). In contrast, our previous results on Ti-Ni superelastic alloy report a degradation ratio of 25.3% after the same number of cycles [37]. In our prior work on Ti–Ni–Cu–Pd bulk materials, we observed that this alloy system is remarkably resistant to introducing dislocations under thermal or load cycling—an inherent characteristic of the system [23-25]. Moreover, the present results also indicate that, aided by the amorphous phase, the crystalline phase seems even more resistant to the introduction of dislocations during cycling. This outstanding cyclic performance highlights the superior functional stability of the ribbon under mechanical fatigue and underscores the critical role of amorphous–crystalline phase synergy in enhancing the stability of Ti-Ni-Cu-Pd ribbons.

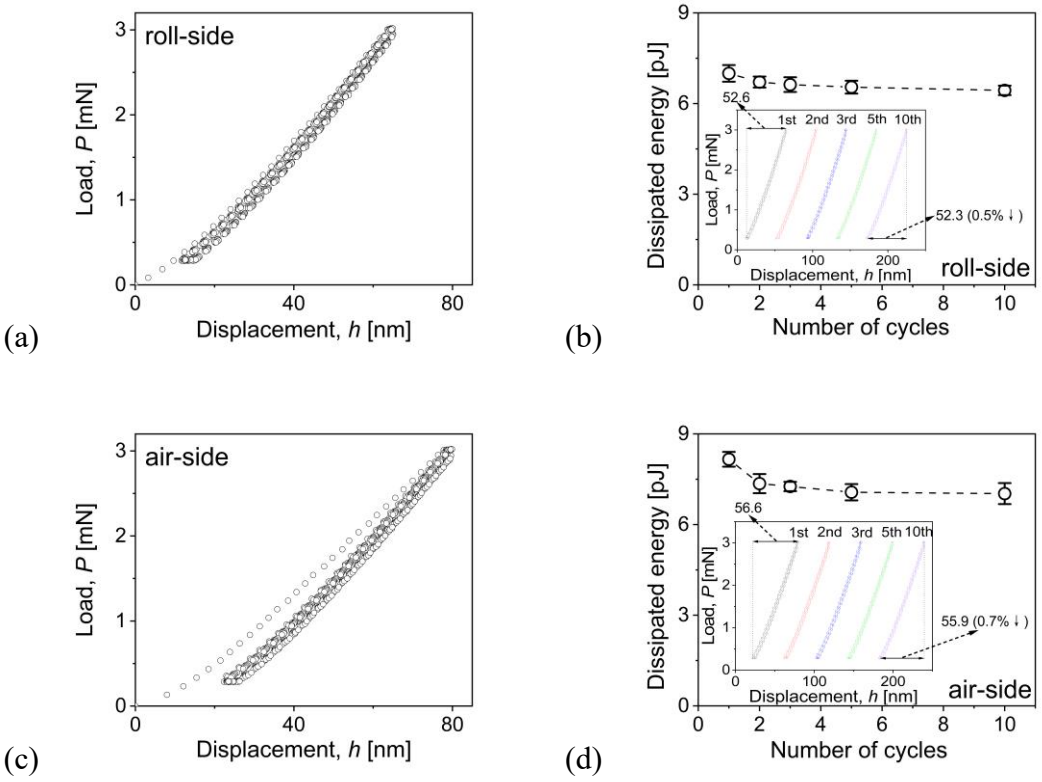


Fig. 4. Results from cyclic indentation tests for the roll and air sides; (a) and (c) representative *P*–*h* curves, and (b) and (d) the dissipated energy as a function of the number of cyclic loading (with inset showing the loading-unloading cycle separately for clarity).

## Conclusion

The gradient Ti-Ni-Cu-Pd SMA ribbon developed in this work demonstrates a unique integration of high strength, large recoverable strain, and excellent cyclic stability under load, attributed to the nanoscale interplay between crystalline and amorphous phases. These findings highlight the effectiveness of nanoscale dual-phase engineering in optimizing functional and mechanical properties of SMAs, offering new avenues for designing high-performance shape memory materials under demanding service conditions.

## Disclosure statement

No potential conflict of interest was reported by the author(s).

**Funding**

This work was supported by the Research Start-up Fund for High-level Talents of Shihezi University under Grant No. RCZK2025111; the China Scholarship Council (CSC) Visiting Scholar Program under Grant No. 201908230066; and the National Research Foundation of Korea (NRF) under Grant Nos. 2022R1A5A1030054 and RS-2023-00273384.

**References**

[1] Bhattacharya K, James RD. The materials is the machine. Science. 2005;307:53-54. doi:10.1126/science.1100892

[2] Miyazaki S, Ishida A. Martensitic transformation and shape memory behavior in sputter-deposited TiNi-base thin films. Mater Sci Eng A. 1999;273-275:106-133. doi:10.1016/S0921-5093(99)00292-0

[3] Wei SS, Zhang JL, Zhang L, et al. Laser powder bed fusion additive manufacturing of NiTi shape memory alloys: a review. Int. J. Extrem. Manuf. 2023;5:032001. doi:10.1088/2631-7990/acc7d9

[4] Safavi MS, Bordbar-Khiabani A, Walsh FC, et al. Surface modified NiTi smart biomaterials: surface engineering and biological compatibility. Curr. Opin. Biomed. Eng. 2023;25:100429. doi:10.1016/j.cobme.2022.100429

[5] Qian H, Umar M, Khan MNA, et al. A state-of-the-art review on shape memory alloys (SMA) in concrete: Mechanical properties, self-healing capabilities, and hybrid composite fabrication. Mater. Today Commun. 2024;40:109738. doi:10.1016/j.mtcomm.2024.109738

[6] Amadi A, Mohyaldinn M, Ridha S, et al. Advancing engineering frontiers with NiTi shape memory alloys: a multifaceted review of properties, fabrication, and application potentials. J. Alloys Compd. 2024;976:173227. doi:10.1016/j.jallcom.2023.173227

[7] Umar M, Qian H, Ali MF, et al. Self-recovery and mechanical behavior of SMAF-

ECC under monotonic and cyclic tensile loading with constitutive model. Constr. Build. Mater. 2025;460:139840. doi:10.1016/j.conbuildmat.2024.139840

[8] Dzogbewu TC, de Beer DJ. Additive manufacturing of NiTi shape memory alloy and its industrial applications. Heliyon 2024;10(1):e23369. doi:10.1016/j.heliyon.2023.e23369

[9] Sidharth R, Celebi TB, Sehitoglu H. Origins of functional fatigue and reversible transformation of precipitates in NiTi shape memory alloy. Acta Mater. 2024;261:120794. doi:10.1016/j.actamat.2023.120794

[10] Umar M, Qian H, Ali MF, et al. Self-healing and flexural performance of SMA fiber-reinforced ECC under freeze–thaw and chloride salt exposure. Constr. Build. Mater. 2025;478:141344. doi:10.1016/j.conbuildmat.2025.141344

[11] Qian H, Du Y, Shi Y, et al. Flexural behavior of RC beams strengthened by novel superelastic NiTi SMA cables grid-reinforced ECC. Eng. Struct. 2025;343:121081. doi:10.1016/j.engstruct.2025.121081

[12] Miyazaki S, Igo Y, Otsuka K. Effect of Thermal Cycling on the Transformation Temperatures of Ti-Ni Alloys, Acta Metall. 1986;34:2045-2051. doi:10.1016/0001-6160(86)90263-4

[13] Tadaki T, Nakata Y, Shimizu K. Thermal cycling effects in an aged Ni-rich Ti-Ni shape memory alloy, Trans JIM. 1987;28:883-890. doi:10.2320/matertrans1960.28.883

[14] Pelton AR, Huang GH, Moinec P, et al. Effects of thermal cycling on microstructure and properties in Nitinol, Mater Sci Eng A. 2012;532:130-138. doi:10.1016/j.msea.2011.10.073

[15] Vanloo FJJ, Bastin GF, Leenen AJH. Phase relations in the ternary Ti–Ni–Cu system at 800 and 870 °C. J. Less-Common Met. 1978;57:111–121. doi:10.1016/0022-5088(78)90167-4

[16] Nam TH, Saburi T, Shimizu K. Cu-content dependence of shape memory characteristics in Ti–Ni–Cu alloys. Mater. Trans., JIM. 1990;31:959–967. doi:10.2320/matertrans1989.31.959

[17] Cui J, Chu YS, Famodu OO, et al. Combinatorial search of thermoelastic shape-

memory alloys with extremely small hysteresis width. Nat. Mater. 2006;5:286–290. doi:10.1038/nmat1593

[18] Zhang ZY, James RD, Müller S. Energy barriers and hysteresis in martensitic phase transformations. Acta Mater. 2009;57:4332–4352. doi:10.1016/j.actamat.2009.05.034

[19] Zarnetta R, Takahashi R, Young ML, et al. Identification of quaternary shape memory alloys with near-zero thermal hysteresis and unpercedented functional stability, Adv Funct Mater. 2010;20:1917-1923. doi:10.1002/adfm.200902336

[20] Khan MT, Li X, Wang S, et al. Fatigue-resistant performance of elastocaloric effect in Ti–Ni–Cu–Pd polycrystalline shape memory alloys. Shap. Mem. Superelasticity. 2025;11:551–560. doi:10.1007/s40830-025-00548-7

[21] Li H, Meng XL, Cai W. Effects of Pd content on microstructures, martensitic transformation of $Ti_{50.5}Ni_{38-x}Cu_{11.5}Pd_x$ (x = 3, 4, 4.5, 5.5) alloys, J Alloys Compd. 2019;791:905-910. doi:10.1016/j.jallcom.2019.03.372

[22] Li H, Meng XL, Cai W. Martensitic transformation and microstructure of (Ni, Cu, Pd)-rich $Ti_{49.5}Ni_{39-x}Cu_{11.5}Pd_x$ alloys with near-zero hysteresis and excellent thermal stability, Intermetallics. 2020;126:106927. doi:10.1016/j.intermet.2020.106927

[23] Meng XL, Li H, Cai W, Hao SJ, Cui LS. Thermal cycling stability mechanism of $Ti_{50.5}Ni_{33.5}Cu_{11.5}Pd_{4.5}$ shape memory alloy with near-zero hysteresis, Scr Mater. 2015;103:30-33. doi:10.1016/j.scriptamat.2015.02.030

[24] Meng XL, Li H, Cai W. Effect of training on the temperature memory effect in $Ti_{49.5}Ni_{34.5}Cu_{11.5}Pd_{4.5}$ shape memory alloy with narrow hysteresis, Scr Mater. 2016;118:29-32. doi:10.1016/j.scriptamat.2016.03.003

[25] Li H, Meng XL, Cai W. Shape memory behaviors in a $Ti_{50}Ni_{33.5}Cu_{12.5}Pd_4$ alloy with near-zero thermal hysteresis, J Alloys Compd. 2018;765:166-170. doi:10.1016/j.jallcom.2018.06.205

[26] Telford M. The case for bulk metallic glass, Mater Today. 2004;7:36-43.

doi:10.1016/S1369-7021(04)00124-5

[27] Johnson WL, Samwer K. A universal criterion for plastic yielding of metallic glasses with a $(T/T_g)^{2/3}$ temperature dependence, Phys Rev Lett. 2005;95:195501. doi:10.1103/PhysRevLett.95.195501

[28] Greer AL, Ma E. Bulk metallic glasses: at the cutting edge of metals research, MRS Bull. 2007;32:611-615. doi:10.1557/mrs2007.121

[29] Shimizu F, Ogata S, Li J. Yield point of metallic glass, Acta Mater. 2006;54:4293-4298. doi:10.1016/j.actamat.2006.05.024

[30] Wang Y, Li J, Hamza AV, Barbee TW. Ductile crystalline-amorphous nanolaminates, Proc Natl Acad Sci USA. 2007;104:11155-11160. doi:10.1073/pnas.0702344104

[31] Shimizu F, Ogata S, Li J. Theory of shear banding in metallic glasses and molecular dynamics calculations, Mater Trans. 2007;48:2923-2927. doi:10.2320/matertrans.MJ200769

[32] Tian L, Cheng YQ, Shan ZW, et al. Approaching the ideal elastic limit of metallic glasses, Nature Commun. 2012;3:609. doi:10.1038/ncomms1619

[33] Delville R, Malard B, Pilch J, et al. Transmission electron microscopy investigation of dislocation slip during superelastic cycling of Ni-Ti wires, Int J Plast. 2011;27:282-297. doi:10.1016/j.ijplas.2010.05.005

[34] Ahadi A, Sun Q. Stress-induced nanoscale phase transition in superelastic NiTi by in situ X-ray diffraction, Acta Mater. 2015;90:272-281. doi:10.1016/j.actamat.2015.02.024

[35] Amini A, Cheng C. Nature of hardness evolution in nanocrystalline NiTi shape memory alloys during solid-state phase transition. Sci. Rep. 2013;3:2476. doi:10.1038/srep02476

[36] Huang X, Nohava J, Zhang B, Ramirez AG. Nanoindentation of NiTi shape memory thin films at elevated temperatures. Int. J. Smart Nano Mater. 2011;2:39–49. doi:10.1080/19475411.2011.558179

[37] Li H, Gao Z, Suh J-Y, Han HN, Ramamurty U, Jang J-i, On the superelastic behavior during spherical nanoindentation of a Ni-Ti shape memory alloy, Materialia. 2024;33:102020. doi:10.1016/j.mtla.2024.102020

[38] Shastry VV, Ramamurty U. Simultaneous measurement of mechanical and electrical contact resistances during nanoindentation of NiTi shape memory alloys, Acta Mater. 2013;61:5119-5129. doi:10.1016/j.actamat.2013.04.049

[39] Shastry VV, Divya VD, Azeem MA, Paul A, Dye D, Ramamurty U. Combining indentation and diffusion couple techniques for combinatorial discovery of high temperature shape memory alloys, Acta Mater. 2013;61:5735-5742. doi:10.1016/j.actamat.2013.06.017

Fig. 1. GI-XRD patterns of as-spun $Ti_{48.5}Ni_{34.5}Cu_{11.5}Pd_{5.5}$ ribbon: (a) roll-side, (b) air-side. (c) HRTEM image, masked fast Fourier transform images and inverse masked fast Fourier transform images of the boxed regions from roll side. (d) HRTEM image, corresponding EDPs calculated by FFT method and inverse masked fast Fourier transform images of the boxed regions from air-side.

Fig. 2. (a) Schematic of the through-thickness gradient architecture. (b) Stress vs. strain rate. Representative *P–h* curves: (c) roll-side (with inset showing a representative 3 mN *P–h* curve without pop-in), (d) air-side.

Fig. 3. Depth recovery ratio as a function of the maximum indentation load (a) and strain (b). (c) Schematic illustrating how two-phase synergy constrains shear band propagation in the amorphous matrix and curbs dislocation slip within the crystals.

Fig. 4. Results from cyclic indentation tests for the roll and air sides; (a) and (c) representative *P–h* curves, and (b) and (d) the dissipated energy as a function of the number of cyclic loading (with inset showing the loading-unloading cycle separately for clarity).